Corrosion Science 222 (2023) 111385



Contents lists available at ScienceDirect

Corrosion Science

journal homepage: www.elsevier.com/locate/corsci





Assessment of corrosive attack of Fe9Cr1Mo alloys in pressurised CO_2 for prediction of breakaway oxidation

Yilun Gong [a,*], Simon P.A. Gill [b], Sabrina Yan [c], Rebecca Higginson [c], Joy Sumner [d], Nigel J. Simms [d], Henrik Larsson [e], Aya Shin [f], Jonathan M. Pearson [f], David J. Young [g], Colin Atkinson [h], Alan C.F. Cocks [i,**], Roger C. Reed [a,i,***]

[a] Department of Materials, University of Oxford, Parks Road, Oxford, OX1 3PH, United Kingdom
[b] School of Engineering, University of Leicester, University Road, Leicester, LE1 7RH, United Kingdom
[c] Department of Materials, Loughborough University, Epinal Way, Loughborough, LE11 3TU, United Kingdom
[d] School of Water, Energy & Environment, Cranfield University, College Road, Bedfordshire, MK43 0AL, United Kingdom
[e] Department of Materials Science and Engineering, KTH Royal Institute of Technology, SE-100 44, Stockholm, Sweden
[f] EDF Energy, Barnett Way, Barnwood, GL4 3RS, Gloucestershire, United Kingdom
[g] School of Materials Science and Engineering, University of New South Wales, Sydney, NSW 2052, Australia
[h] Department of Mathematics, Imperial College, London, SW7 2BZ, United Kingdom
[i] Department of Engineering Science, University of Oxford, Parks Road, Oxford, OX7 6DP, United Kingdom

ARTICLE INFO

Keywords:
Oxidation
Carburisation
Breakaway
Modelling
Characterisation
Lifing

ABSTRACT

To provide clarity on the poorly-understood mechanism of breakaway oxidation, corrosion of Fe9Cr1Mo steel in pressurised CO_2 is quantified and modelled. The temperature range 400–640 °C, relevant to nuclear power plants, is emphasised. Attack is in the form of combined oxide scale growth and internal carburisation of the metal. Carbon activity in the metal at its surface exhibits a strong time dependence consistent with the kinetically-limited transport of carbon due to the slow Boudouard reaction. Breakaway is associated with the approach to saturation of the steel with respect to carbon. Diffusion modelling agrees well with steel carbide precipitation observations.

1. Introduction

Corrosion of 9Cr steels in high-pressure CO_2-rich gaseous environments causes both carburisation and oxidation to occur in a coupled manner [1]. This situation makes the prediction of degradation – which is important for the assessment of component failure – very challenging. Currently, there is a growing worldwide interest in such chemical attacks, because of the recognition of the advantages of using pressurised CO_2 in advanced thermodynamic plant being designed and constructed based upon the Brayton or Allam power cycles [2]. There is also an urgent need for studies of alloy stability for CO_2 gas sequestration and for applications involving concentrated solar power [3–5]. CO_2 is also used as a coolant in some breeds of nuclear plant [6], such as the advanced gas-cooled reactors (AGRs, Fig. 1) which have been running in the United Kingdom since the 1980s, making the behaviour of 9Cr steels in such environments of significant practical importance [7–9]. Moreover, CO_2 is assuming importance for space exploration, for example to Mars or Venus, since it is often the prevailing gaseous species on planetary systems other than Earth [10–12].

What are the important characteristics of corrosive attack by CO_2? On the one hand, one observes the rapid formation of oxide species in a manner broadly similar to that observed in low oxygen content environments such as H_2O [13–15] or CO_2. For example, for the Fe9Cr1Mo ferritic steels used in the AGR nuclear reactors which are studied here, outward and inward growing scales of magnetite and Cr-rich spinel are found [8,16]. But the underlying metal is also carburised as evidenced by the extensive formation of carbide phases which then subsequently experience oxidation [8,17]. The balance of attack due to oxidation and carburisation depends upon the temperature and

* Correspondence to: Max–Planck-Institut für Eisenforschung, Max–Planck-Straße 1, Düsseldorf 40237, Germany.
** Corresponding author.
*** Corresponding author at: Department of Materials, University of Oxford, Parks Road, Oxford, OX1 3PH, United Kingdom.
E-mail addresses: yilun.gong@materials.ox.ac.uk, y.gong@mpie.de (Y. Gong), alan.cocks@eng.ox.ac.uk (A.C.F. Cocks), roger.reed@eng.ox.ac.uk, roger.reed@materials.ox.ac.uk (R.C. Reed).

https://doi.org/10.1016/j.corsci.2023.111385
Received 18 May 2023; Received in revised form 4 July 2023; Accepted 6 July 2023
Available online 11 July 2023
0010-938X/© 2023 The Author(s). Published by Elsevier Ltd. This is an open access article under the CC BY license (http://creativecommons.org/licenses/by/4.0/).

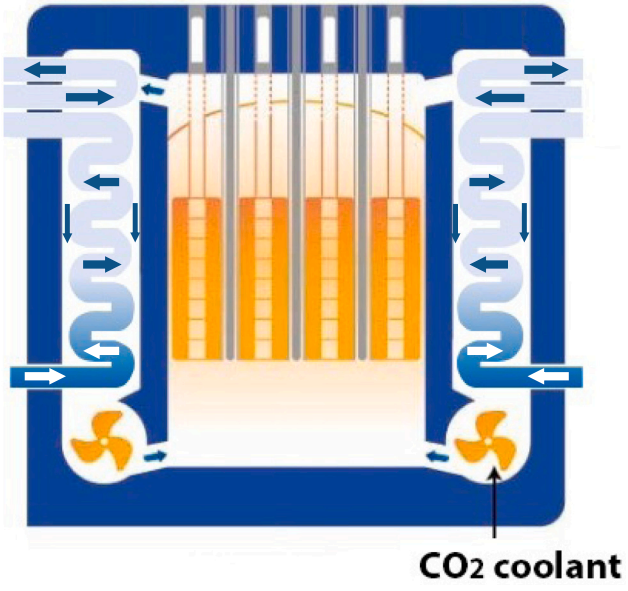


Fig. 1. Schematic Advanced Gas-cooled Reactor (AGR).

presumably also the CO_2 pressure, although experimental data are sparse. Of prime importance is the mechanism of carbon transport across the oxide scale, for which there is no consensus at present [18], short of an acknowledgement that the catalysis of a rather sluggish Boudouard reaction is needed, particularly as the temperature falls below 500 °C [19]. Therefore, it is the quantification of the carbon activity, particularly at the metal/scale interface which is one of the overarching and outstanding scientific challenges [8,20].

In this paper, the corrosion of Fe9Cr1Mo ferritic steel in high-pressure CO_2 is considered, under conditions relevant to the AGR reactors in use in the UK. The paper is constructed in the following way. First, the behaviour of this steel in the temperature range of 400 to 640 °C is considered; in this range, the balance of attack due to oxidation and carburisation is studied, particularly in the context of so-called breakaway oxidation. Next, mathematical modelling is carried out with an emphasis on the carburisation step and the variation of the carbon activity at the metal/scale interface; it is shown that there is a strong time dependence to this which needs to be accounted for if accurate predictions are to be made. The effects of component geometry and metal loss due to oxidation are considered and rationalised. The Robin-type boundary condition then needs to be modified to account for the moving oxide/metal scale interface. In the final part of the paper, the implications of our findings are considered, particularly in relation to the use of Fe9Cr1Mo steel for these applications, and the risk of breakaway attack occurring in the lower temperature regime, which is pertinent to AGR reactor conditions.

The context of the work reported here relates to the phenomenon of so-called breakaway oxidation of Fe9Cr1Mo steel which causes a departure from parabolic oxidation kinetics towards a more aggressive linear attack. Whilst this effect has been known for some years, details of the mechanism remain controversial. On the one hand, breakaway oxidation has never been observed at temperatures close to the conditions of the AGR reactors; nonetheless, it is seen under accelerated testing conditions which typically involves the use of temperatures higher by at least 100 °C. Statistical approaches based upon weight gain data are currently employed to assess breakaway oxidation, but this can be criticised because of its blind empiricism. An alternative approach – which is followed in this paper – is to focus on the damage caused by carburisation (rather than oxidation) since carburisation could act as a precursor to breakaway oxidation and also potentially would alter the mechanical response of the structural component. It is noted that as the degree of carburisation increases at the alloy surface the concentration of chromium available in the ferrite phase for scale formation is decreased, until a protective scale cannot be maintained.

2. Experimental procedures and results

2.1. Gas exposure experiments

An extensive programme of experimental work has been made available for the present work by EDF Energy (formerly British Energy) to study the mechanisms of breakaway oxidation for experimental 9Cr steels under various exposure conditions [21]. Three distinct sets of experiments are selected in this study which employed carefully controlled experimental conditions over the temperature range of 400–600 °C with exposure to CO_2 environment up to 114 kh.

The first set consists of Fe9Cr1Mo ferritic steel finned samples (see material HRA1542 in Table 3) exposed to high pressure CO_2 (at a gauge pressure of ~41.4 bar) at temperatures between 580 and 640 °C. These are referred to here as **Group I**. This part of the experimental dataset – and the sample preparation and exposure procedures – has also been considered in Gong *et al.* [8]. Details of gas compositions, exposure duration and temperatures for a subset of these samples are listed in Table 1 (samples 11–18). Autoclaves (inner volume of ~22.5 L) were used. The gas compositions are listed in Table 2 as Gas 3 and 4. A gas flow rate of 20 mL/min at standard temperature and pressure (STP) was used. Readers are referred to Gong *et al.* [8] for more details. The time-to-breakaway (ttb) is estimated as a time interval between the last visual inspection with no breakaway (TTB) and the next inspection (TafterB). The mass gain data (of the full dataset) is summarised in Fig. 3: higher temperatures give larger weight gains and lower ttb; samples exposed to the higher moisture content (gas 4) show slightly larger weight gains. The probability distribution of TTB/TafterB, for all 98 samples with observed breakaways, can be found in Appendix A Supplementary data.

A second set of Fe9Cr1Mo finned samples is considered here, see materials 256 and 277 in Table 3. Data acquired for these samples is referred to as **Group II**, which were exposed at the low end of the temperature range of interest, i.e. ~400 to 520 °C (see Table 1) [23]. The 2D/3D geometry of the component considered is illustrated in Fig. 2. These were sectioned with 4 or 6 fins along the length, with surfaces wet-ground to 180 grit SiC, before being degreased in hot Genklene (inhibited 1.1.1 trichloroethane) in an ultrasonic bath, followed by an acetone wash. Specimens of material 256 were contained in annular stainless steel or silver trays mounted on the normal specimen support assemblies in the British Nuclear Design and Construction (B.N.D.C.) small autoclaves, while specimens of material 277 were located in rectangular stainless steel or Inconel 600 containers which were in turn situated in perforated stainless steel or nickel cages (larger autoclaves). A gas mixture with the gas 2 composition listed in Table 2 was employed in tests. The gas flow rate through the autoclaves was controlled at 25 mL/min (measured at laboratory pressure). The gas was pre-mixed to the desired composition, except moisture which was regulated by means of a saturated molecular sieve humidifier [23].

The third set of experimental data is for Fe9Cr1Mo steels in a plain tube geometry. These are referred to as **Group III**. They were also exposed at low temperatures [24]. The material has a slightly higher lower limit of silicon content, see material 283 in Table 3. Samples were cold-finished, normalised and annealed at 850 to 875 °C for one hour followed by furnace cooling at a rate slower than 43 K h^{-1} to 680 °C. Both heat treatments were carried out in a protective atmosphere. The final finishing of the outer surface was by grit blasting with 60–80 mesh alumina grit. Samples were dry-machined before being ultrasonically degreased in Genklene, contained in recrystallised alumina crucibles and weighed until a constant weight was achieved. Exposure was carried out in the large autoclaves used for **Group II** samples, using the gas 3 composition listed in Table 2. Detailed exposure duration and the conditions for each sample are listed in Table 1 (samples 6–10).

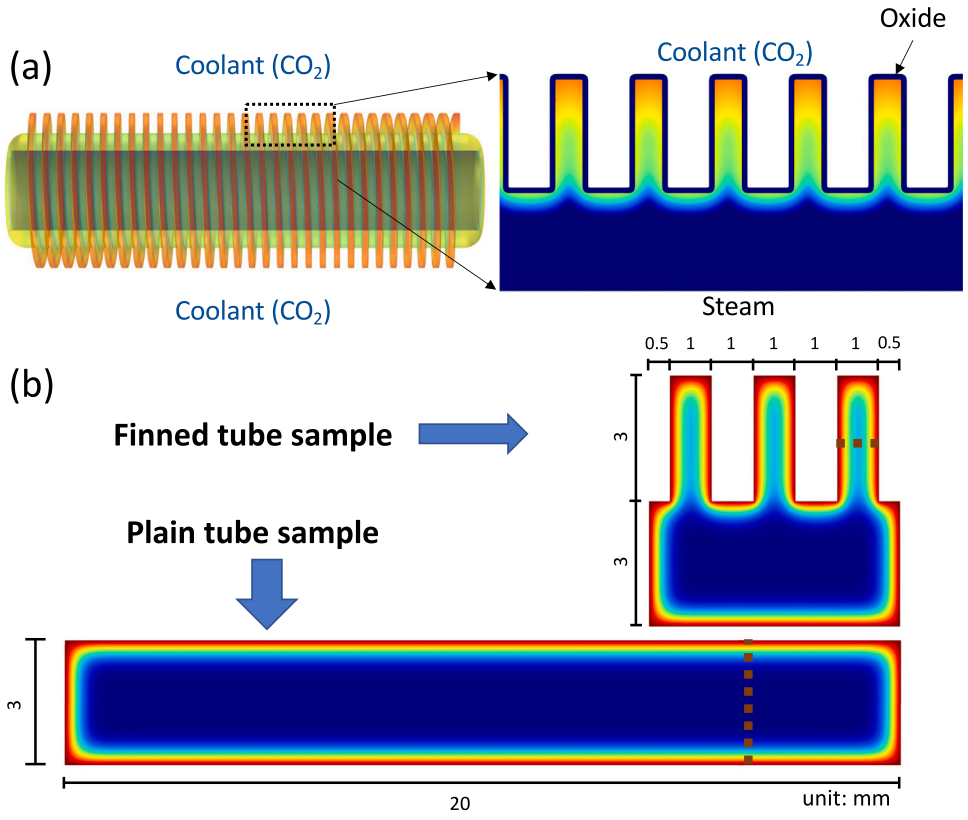


Fig. 2. (a): Illustration of the experimental finned and plain tube sample geometry; (b): dimensions of the finned tube and plain tube samples with illustrative carbon concentration fields; samples are profiled across the fin tip and the tube base as illustrated in dashed brown lines.

Table 1
Summary of samples for microstructural characterisations.

Group	Sample ID	Sample name	Materials code	Geometry	Duration [kh]	Temperature [°C]	Gas composition	Protective/ Breakaway
II	1	HRA2825	277	Finned	97.02	450	1	Protective
II	2	HRA4689	256	Finned	90.1	400	1	Protective
II	3	HRA2803	277	Finned	113.598	485	1	Protective
II	4	HRA2270	256	Finned	132	520	1	Protective
II	5	HRA2837	277	Finned	115	520	1	Protective
III	6	HRA4693	283	Plain Tube	90.1	400	2	Protective
III	7	HRA3857	283	Plain Tube	94.02	450	2	Protective
III	8	HRA3890	283	Plain Tube	110.598	485	2	Protective
III	9	HRA3868	283	Plain Tube	112	520	2	Protective
III	10	HRA3879	283	Plain Tube	98.605	550	2	Protective
I	11	HRA8525	HRA1542	Finned	5.845	600	3	Protective
I	12	HRA8185	HRA1542	Finned	1.715	640	4	Breakaway[a]
I	13	HRA8185	HRA1542	Finned	0.76	640	4	Protective
I	14	HRA8185	HRA1542	Finned	0.504	640	4	Protective
I	15	HRA8183	HRA1542	Finned	0.76	640	3	Protective
I	16	HRA8183	HRA1542	Finned	0.504	640	3	Protective
I	17	HRA8526	HRA1542	Finned	10.865	600	3	Breakaway[b]

[a]All three fins are close to breakaway.
[b]Left fin is protective while the middle and right fins are close to breakaway.

Table 2
Summary of exposed gas compositions.

Gas number	H_2O [ppmv]	H_2 [ppmv]	CH_4 [ppmv]	CO [vol%]	CO_2
1	625	300	700	1	Bal.
2	625	200	700	1	Bal.
3	300	100	300	1	Bal.
4	700	100	300	1	Bal.
5	1100	100	300	1	Bal.

2.2. Dimensional metrology of oxide layers

Typical duplex oxide microstructure developed in these samples has been reported in our previous paper [8]. Here further addition, careful measurements of oxide dimensions have been conducted for all selected samples following the procedures in Ref. [25]: optical microscopic images across the whole oxidised surface have been taken for each sectioned sample, with relative positions obtained from an x–y calibrated microscope stage; collected images were then automatically analysed, allowing the statistical distribution of thickness for each

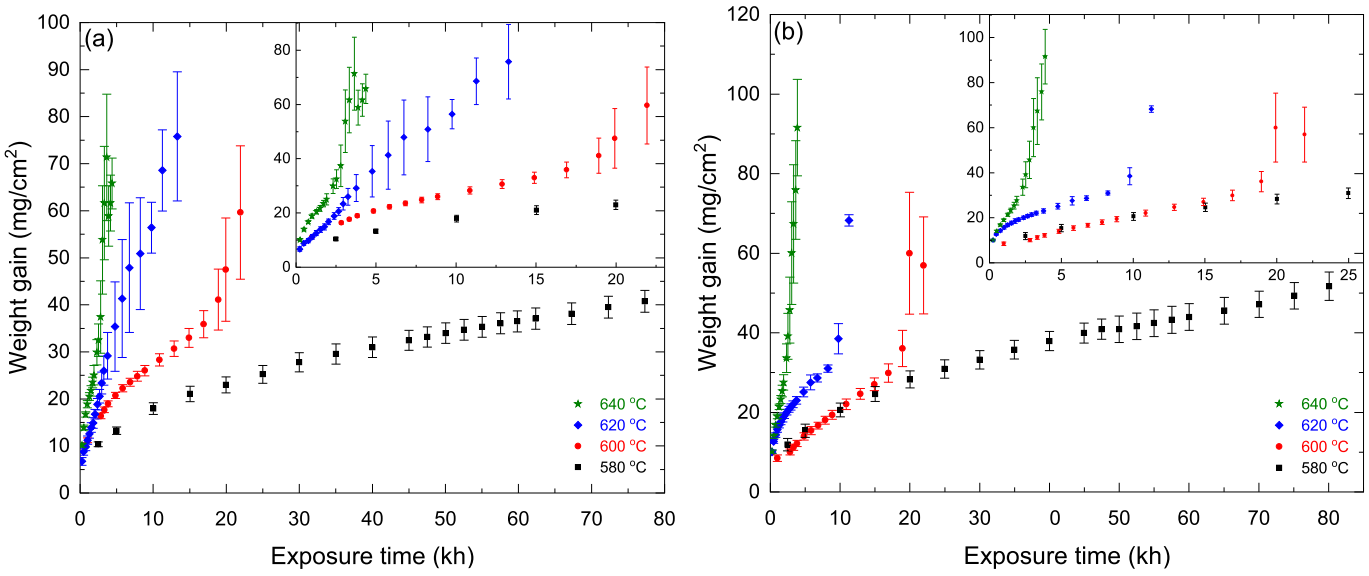


Fig. 3. Weight gains of material HRA1542 exposed to (a) gas composition 3 [8] and (b) gas composition 4 [22], at 580 °C (black), 600 °C (red), 620 °C (blue) and 640 °C (green); one standard deviation from repeated tests is used to evaluate uncertainties. (For interpretation of the references to colour in this figure legend, the reader is referred to the web version of this article.)

Table 3
Compositions (wt.%) and area fraction of carbides measured for samples before the exposure (virgin conditions); compositions are measured by inductively coupled plasma optical emission spectrometry (ICP-OES) analysis or combined with the combustion method.

Group	Materials code	C	Si	Mn	P	S	Cr	Mo	Ni	N	Cu	Co	Fe	Carbide area fraction
I	HRA1542	0.093	0.67	0.47	0.011	0.008	9.2	1.04	0.21	–	0.16	0.02	Bal.	2.5±0.4
II	256	0.11	0.63	0.48	0.01	0.004	9.44	0.95	0.15	0.026	–	–	Bal.	2.7±0.5
II	277	0.1	0.61	0.52	0.013	0.005	8.92	1.05	0.17	0.016	–	–	Bal.	2.5±0.3
III	283	0.11	0.69	0.4	0.016	0.01	9.34	0.98	0.23	0.015	–	–	Bal.	2.5±0.4

oxide layer to be analysed. Features such as oxide spallation can be well characterised by such analysis. Additionally, a set of data from British Nuclear Design and Construction (now Jacobs), where the oxide thicknesses are measured either by incremental surveys or by random measurements, is included in the current assessment; increments for the surveys were between 100 and 250 μm [26]. All measured data are summarised in Fig. 4.

2.3. Microstructure of the substrate and quantifications of carbon uptake

Fig. 5 summarises the typical microstructure of the substrate close to the spinel/substrate interface across the range of exposure times and temperatures (at the protective stage) being studied. The carbide precipitates due to carbon uptake are revealed as dark regions in the figure, imaged by ion-induced secondary electron signals. Selected area diffraction (SAD) by transmission electron microscope (TEM) suggests these particles consist of $M_{23}C_6$, M_7C_3 and M_2C carbides [8,27,28]. One can see an increased amount of carbide precipitates with longer exposure times and/or higher temperatures.

To quantitatively evaluate the carbon uptake in the substrate, the spatial distribution of the area fraction of carbide was measured for each sample. Because system errors are inevitable, exposure conditions (including temperature and time) have been chosen such that the expected variance of carbon content distribution (within a single specimen) is maximised and the relative error of measurements within a single specimen is minimised. All selected samples were first polished to 0.04 μm surface finish (colloidal silica was used as the final polishing solution), followed by careful surface cleaning using both water and methanol, then air drying. To achieve a high contrast differential between the carbide and the matrix, a reactive gas-enhanced ion beam-induced secondary electrons imaging method (carried out on the Thermo Fisher (formerly FEI) Nova 600 NanoLab Dual Beam (FIB-FEGSEM) system) was used. The procedure involved collecting an image with the reactive gas valve closed and then a second image with the valve open, this second image was used for analysis. A XeF_2 reactive gas was used with a probe current of 0.5 nA (30 kV) and a frame time of 47.6 s. A horizontal field width of 50 μm was chosen for each image and the stage was moved in 50 μm increments perpendicular to the scale/alloy interface so that a continuous line of images containing the particles was collected. The particles in the images were quantified using a threshold-based binarisation method using the ImageJ software. All images were manually thresholded and checked; artefacts such as pores were excluded from the analysis. Readers are referred to [29] for more details on the quantitative analysis of carbide particles. The measured fraction of carbide precipitates has been converted to carbon concentration (or molar fraction) assuming that local phase assemblage comes to local equilibrium. This is done by using the CalPhaD approach with all possible phases included in the Thermo-Calc steel and Fe-alloys database (TCFE8). Readers are referred to Appendix A Supplementary data for all measured carbon profiles.

It should be emphasised that the upper limit of the vertical axis in Fig. 5, corresponding to long-term exposures (more than 20 years), is currently inaccessible by experiments; thus the exact amount of carbon uptake corresponding to the breakaway condition in the low-temperature regions (right-hand side of the figure) is not available from experiments.

3. Description of modelling approach

The above experimental observations motivate the proposed kinetic model for lifetime assessment. On exposure to a CO/CO_2 gaseous

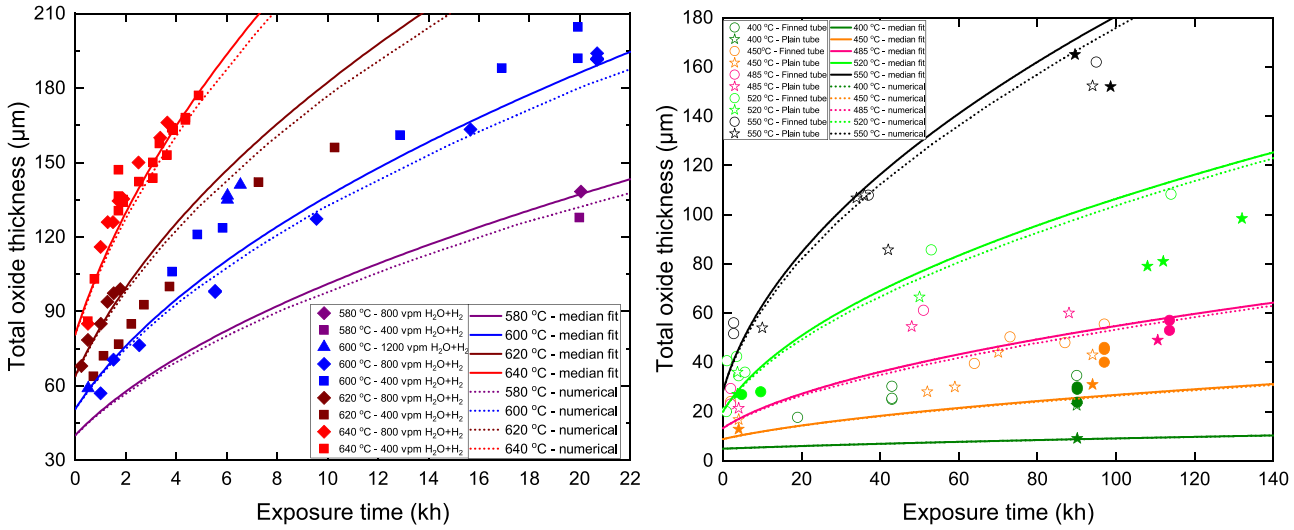


Fig. 4. Comparisons of measured total oxide thickness (solid symbols by this work and hollow symbols from [26]) against analytical fittings (parabolic) and numerical simulations (dashed lines); finned tube samples (solid circles) and plain tube samples (solid star) are exposed at temperatures of 400 °C (olive), 450 °C (orange), 485 °C (pink), 520 °C (green), 550 °C (black), 580 °C (purple), 600 °C (blue), 620 °C (wine) and 640 °C (red); samples above 550 °C are exposed to gas 3 (solid squire), gas 4 (solid diamond) and gas 5 (solid triangle) while samples below 580 °C are exposed to gas 1 (finned samples) and gas 2 (plain tube samples). The median of oxide thickness from measurements is considered here. (For interpretation of the references to colour in this figure legend, the reader is referred to the web version of this article.)

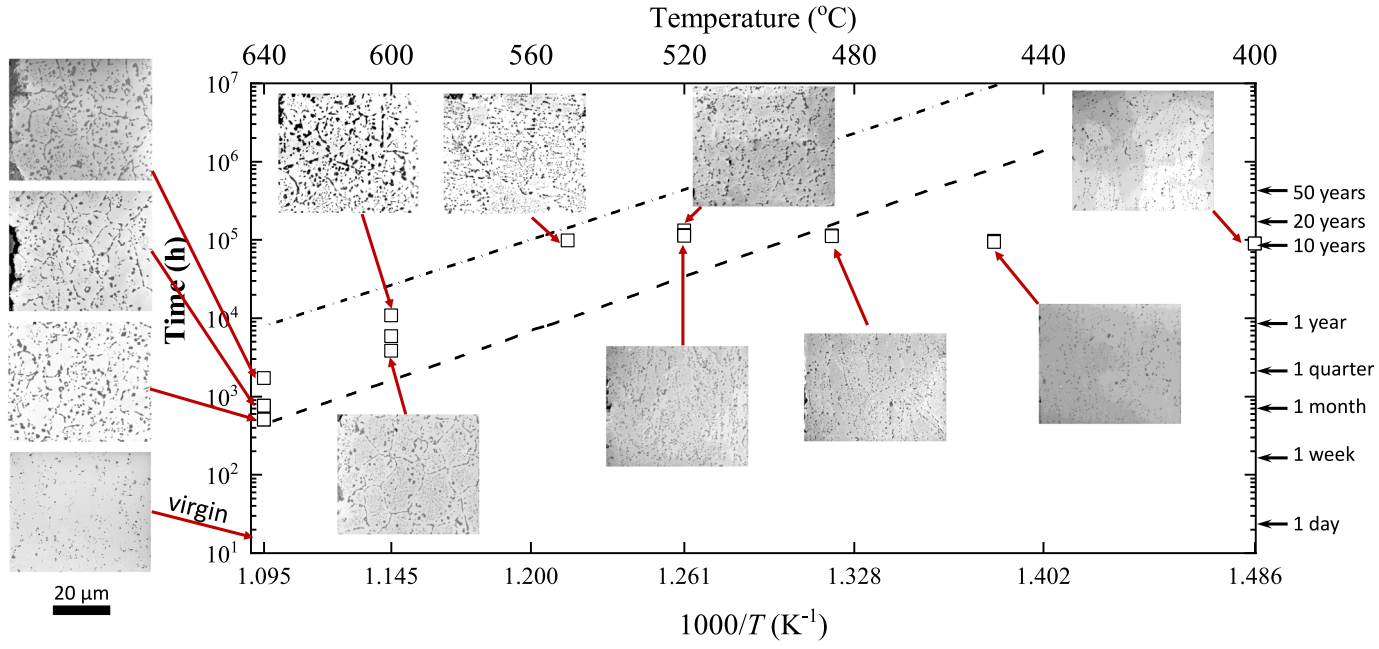


Fig. 5. Typical ion-induced secondary electron images collected at the spinel/substrate interface, for samples exposed at different combinations of temperature and time; the bottom left image shows the virgin condition (prior to CO_2 exposure). To guide the eye, predicted time of carbon saturation with $\eta_C^{crit} = 0.2$ and $\eta_C^{crit} = 0.9$ (using the Arrhenius fit of both α_a/V_m and ζ for a 1D domain corresponding to the fin width, considering oxidation kinetics, see Section 4) are shown as the dashed dot line and the dashed line, respectively.

environment, steels develop a duplex scale consisting of magnetite and Cr-rich spinel layers, accompanied by precipitation of Cr-rich carbides within the underlying substrate, see the illustration of phase transformations in Fig. 6. The boundary condition applied at the spinel/substrate interface, the modelling of carbon diffusion in the substrate, and their coupling with oxidation kinetics are described in this section. Compared with the previous modelling works by the authors [8,30], the method adopted here is more robust and more efficient; this is particularly useful for lifing purposes where the model needs to be trained and calibrated against a large amount of experimental data.

Time integration of the system of equations which results is performed numerically, using non-linear General Partial differential equation (PDE) solvers implemented in the COMSOL® v. 5.4 software package.

3.1. The interface reaction at the spinel/substrate interface

No attempt has been made to account for the transport of carbon through the oxide scale, for which inadequate information is available; instead boundary conditions for carbon describing the chemical (Boudouard) reaction at the spinel/substrate interface [19] (or across

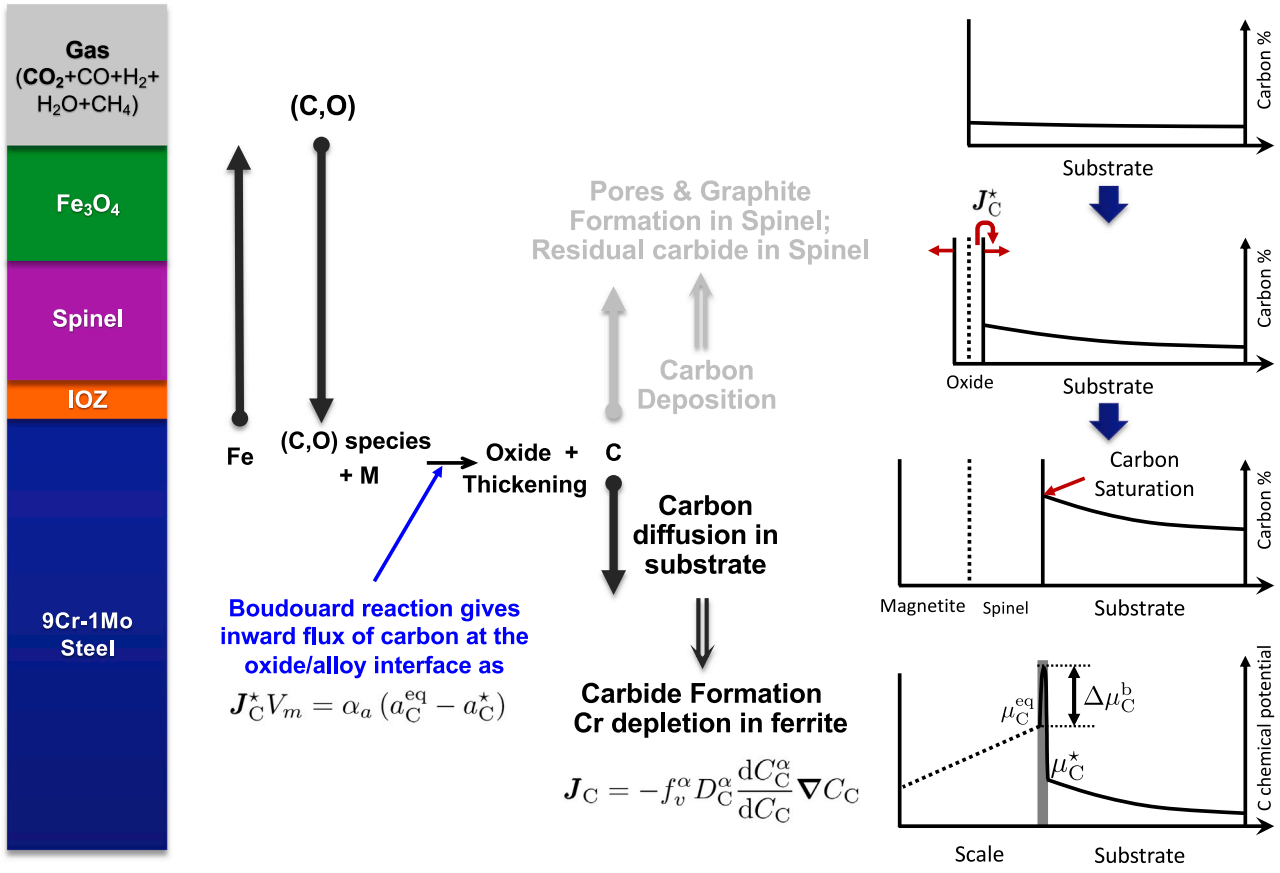


Fig. 6. Illustrations of phase transformations in CO_2 oxidation of 9Cr1Mo steel. The distribution of the chemical potential of carbon is shown at the bottom right.

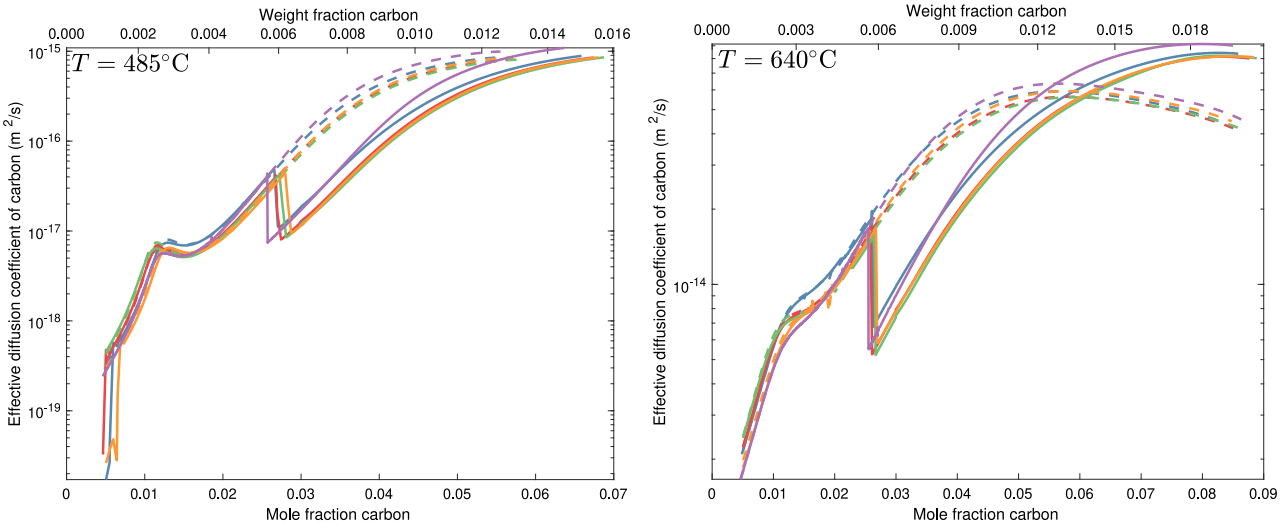


Fig. 7. Calculated effective diffusion coefficient of carbon as a function of total fraction of carbon up to $a_C = 1$; calculations were done either by considering all possible phases (solid lines) or only including the $M_{23}C_6$ type of carbide (dashed lines), with the composition of alloy 277 (blue), 283 (red), 256 (green), HRA1542 (orange) and Fe-9Cr1Mo (purple); the weight fraction of carbon is converted from the molar fraction of carbon based on the Fe-9Cr-1Mo alloy composition. (For interpretation of the references to colour in this figure legend, the reader is referred to the web version of this article.)

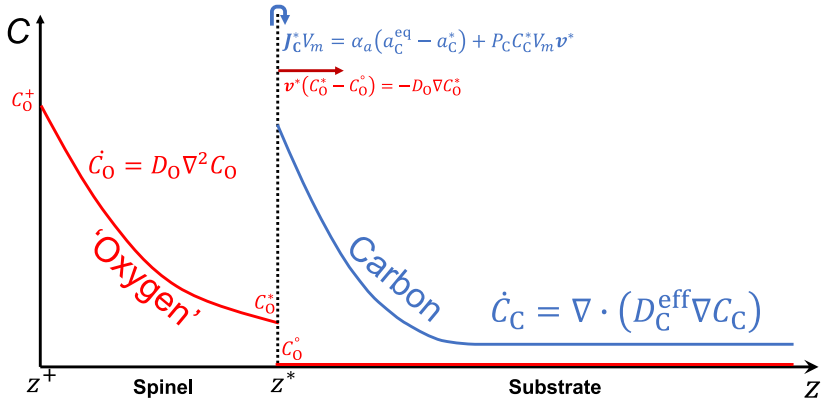


Fig. 8. Illustration of coupling between oxidation with carburisation kinetics. The internal oxidation zone (IOZ, shown in Fig. 6) is omitted here because carbon diffuses through the Cr-depleted matrix of the IOZ rapidly and without reaction; its activity at the IOZ/carburisation zone interface is therefore very little changed from the value at the scale/metal interface.

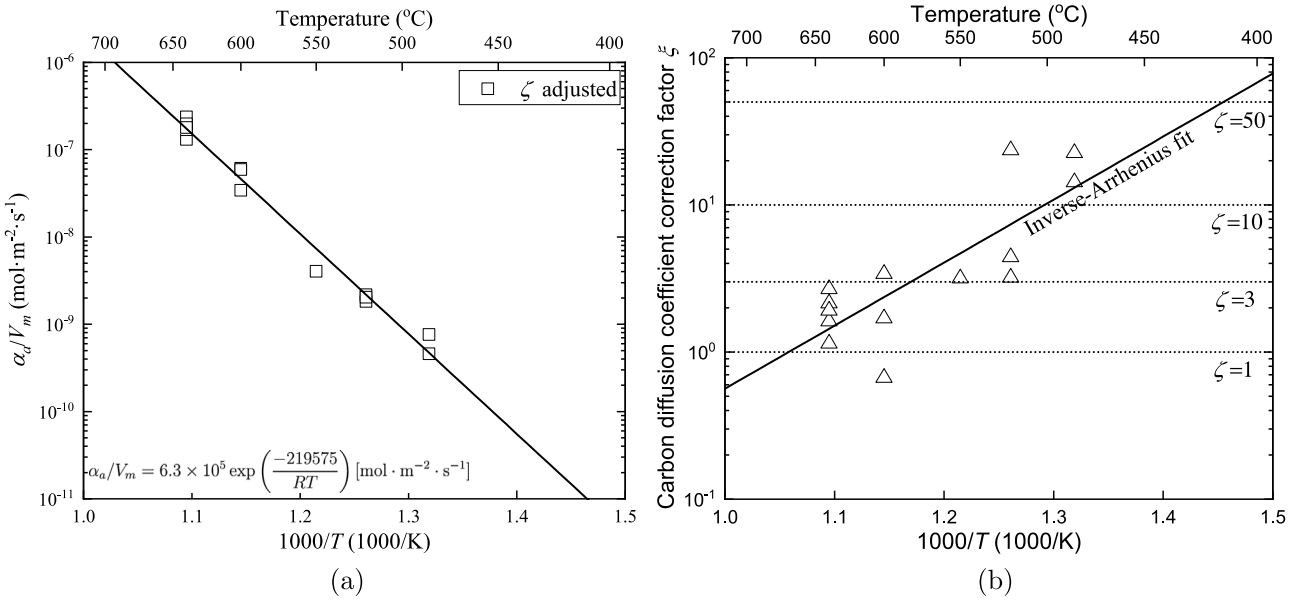


Fig. 9. Derived α_a/V_m (a) and ζ (b) for each sample by allowing ζ to be adjusted for each fitting of profiles; black lines show the (inverse) Arrhenius fit of α_a/V_m and ζ over the temperature. Calculations were done without taking into account oxidation kinetics.

the whole oxide layers):

$$CO_2 = CO + {}^1/_2\,O_2 \qquad 2CO = CO_2 + C \tag{1}$$

is assumed where the inward flux of carbon $\boldsymbol{J}_C^\star$ has the functional form consistent with [30]:

$$\boldsymbol{J}_C^\star V_m = \alpha_a \{T\} \left(a_C^{eq} - a_C^\star\right) \tag{2}$$

Here V_m denotes the alloy molar volume; α_a [m s^{-1}] the interface reaction coefficient of carbon which is assumed to follow an Arrhenius law; a_C^{eq} and $a_C^\star$ are the carbon activity at equilibrium (determined by the Boudouard reaction) and instantaneously at the spinel/substrate interface respectively. A schematic chemical potential profile for carbon is shown at the bottom right of Fig. 6. A detailed justification of Eq. (2) by applying absolute reaction rate theory is provided in Gong *et al.* [30].

3.2. The diffusion of carbon in the substrate

The diffusion of substitutional elements such as chromium is sluggish compared with that of carbon. This gives rise to significant (long-range) chemical inhomogeneity within the substrate only with respect to carbon. The diffusion problem can therefore be simplified by considering only the diffusion of carbon. The flux of carbon is driven by the gradient of the carbon concentration within the ferrite matrix, C_C^α. It proves convenient, however, to express the diffusion equation in terms of the total carbon concentration C_C (i.e. that in solution in the ferrite matrix, plus the carbon tied-up in the precipitates, whose volume fraction evolves with time). We assume that the precipitation kinetics is sufficiently rapid such that a state of local equilibrium is achieved. The rate of evolution of the carbon concentration C_C is then given by

$$\dot{C}_C = \boldsymbol{\nabla} \cdot \left(D_C^{eff} \boldsymbol{\nabla} C_C\right) \tag{3}$$

where D_C^{eff} is an effective diffusion coefficient, expressed by

$$D_C^{eff} = f_v^\alpha D_C^\alpha \frac{dC_C^\alpha}{dC_C} \tag{4}$$

where f_v^α is the volume fraction of ferrite and D_C^α is the chemical diffusion coefficient of carbon in ferrite. For a given alloy composition and total carbon concentration, f_v^α and D_C^α can be determined using the thermodynamic database. This allows the gradient $\frac{dC_C^\alpha}{dC_C}$ and therefore D_C^{eff} to be calculated. Fig. 7 shows calculated values of D_C^{eff} as a

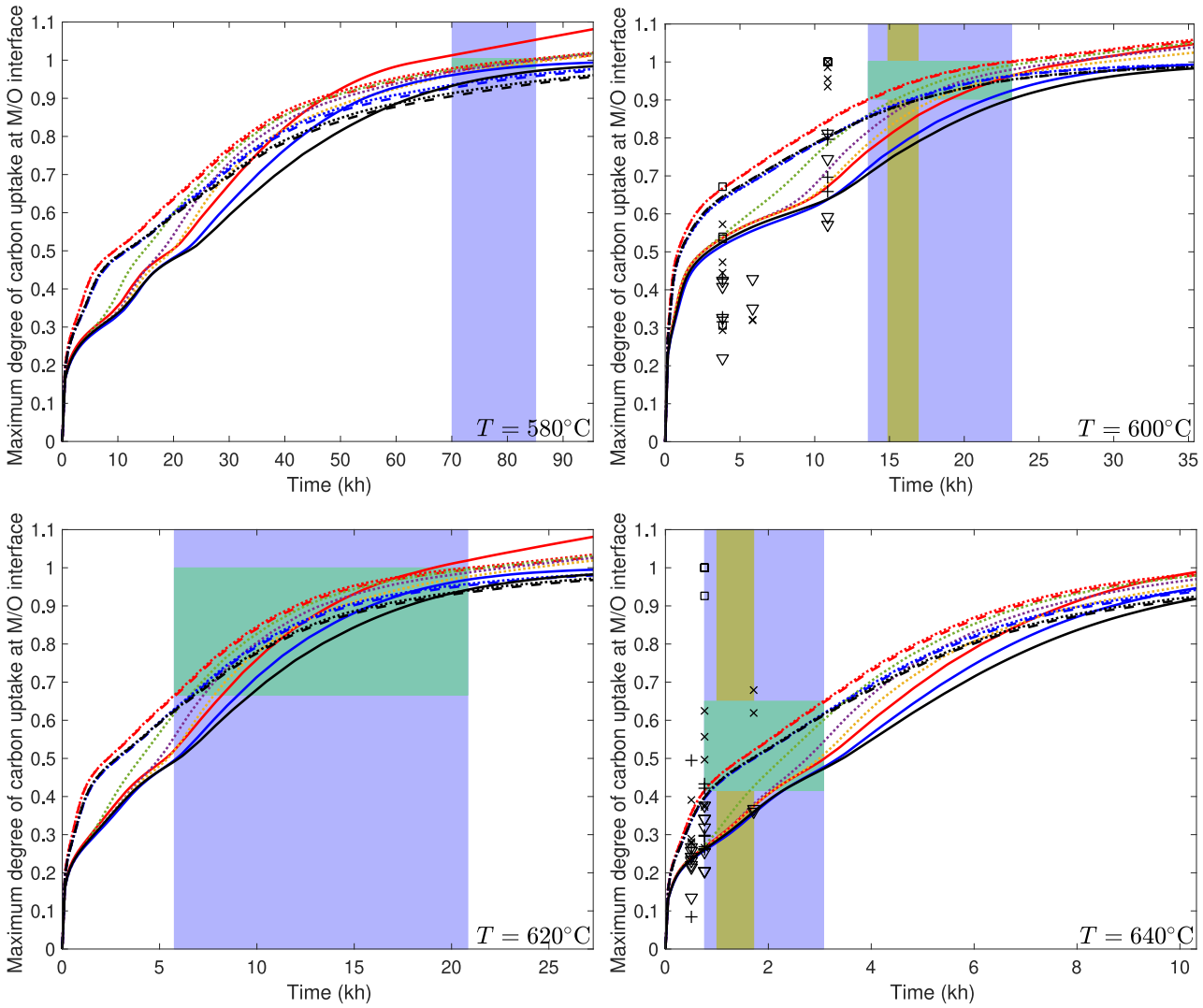


Fig. 10. Predicted maximum degree of carbon uptake of the 9Cr-1Mo alloy taking into account oxidation kinetics with $P_C = 1$ (red) and $P_C = 0$ (blue), and without taking into account oxidation kinetics (black); calculations have been done in both 1D (solid lines) and 2D (planar: dashed lines; axisymmetric: short dot lines), with geometry defined in Fig. 12. Values of α_a/V_m and ζ follow the best fit of for each temperature as outlined in Section 4. The yellow and blue regions cover the range of measured ttb for samples listed in Table 1 and Fig. 3 respectively. The green rectangle shows the range of η_C^{crit} predicted by the 2D axisymmetric model (with $P_C = 1$) in the ttb zone (for the larger dataset). Measured carbon mole fraction at the spinel/substrate interface (converted to the degree of carbon uptake) at 0 (□), 0.5 (×), 1 (+) and 1.5 mm (▽) away from the fin tip are included, compared to predictions at 0.5 (green dot lines), 1 (purple dot lines) and 1.5 mm (orange dot lines) away from the fin tip. (For interpretation of the references to colour in this figure legend, the reader is referred to the web version of this article.)

function of total molar fraction of carbon X_C, at 485 and 640 °C, for different alloys. Discrepancies of D_C^{eff} have been found between those calculated from Eq. (4) and those derived from carbon uptake measurements, particularly at low temperatures. A possible reason involving precipitation-induced strain in the ferrite has been proposed in previous work [30,31]. Due to a lack of relevant measurements, a temperature-dependent correction factor $\zeta\{T\}$ (fitted to carbon profile measurements) is thus introduced here, giving the corrected effective diffusion coefficient of carbon as:

$$D_C^{eff,corr} = \zeta\{T\}\, D_C^{eff} \tag{5}$$

The above models have been coupled with the Thermo-Calc thermodynamic database TCFE8 and the mobility database MOBFE4. The numerical implementation has been tested against the homogenisation model [32–35] as implemented in the DICTRA software package where diffusion of multi-components in multi-phases is explicitly solved in a lattice-fixed-frame of reference. For temperatures ranging from 400 to 640 °C and α_a/V_m from 10^{-14} to 1×10^{-6} mol m^{-2} s^{-1}, predictions using Eq. (3) and DICTRA are within ±5% for the concentration profile and ±10% for the time for carbon saturation (TCS, defined in Section 5). Readers are referred to Appendix A Supplementary data for detailed implementation of DICTRA and its comparisons with the present work.

3.3. The coupling with oxidation kinetics

The duplex scale consists of a Fe-rich magnetite/spinel and a Cr-rich spinel phase region; the former contains very little Cr and grows outwards while the latter contains a Cr concentration similar to the metallic substrate and grows inwards [16,36–38]. The position of the magnetite/spinel interface remains the same as the original gas/substrate interface, and both oxide layers have approximately equal thicknesses [8], as illustrated in Fig. 6. To account for the influence of (inward) growth of the spinel phase on the carburisation kinetics, a moving interface boundary condition is applied at the spinel/substrate interface with its velocity depending on the local concentration gradient of 'an oxygen-containing species' in the oxide at the oxide/alloy interface [39,40]; this is to model the consumption of the substrate, as illustrated in Fig. 8. One should note that the internal oxidation zone (IOZ) is omitted

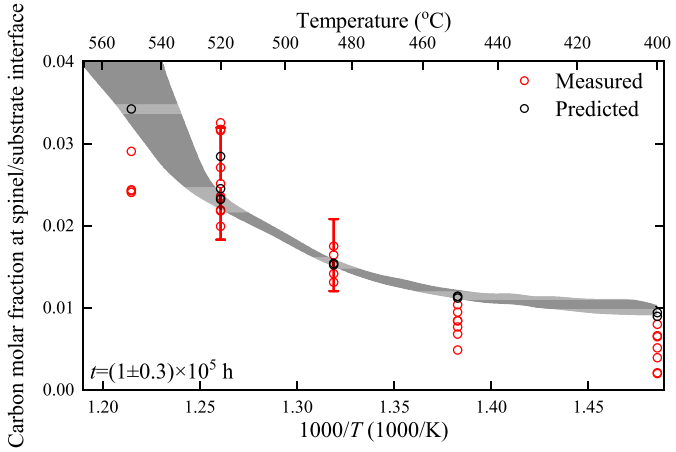


Fig. 11. Comparison of the molar fraction of carbon at the spinel/substrate interface by measurements and predictions; the Arrhenius fit of both α_a/V_m and ζ are used in the carbon uptake model, with oxidation kinetics considered; the grey region is outlined by predictions considering a 1D geometry corresponding to the fin width or the thickness of the plain tube, for different virgin alloys at around 1×10^5 h; the error of measurement at 485 and 520 °C is estimated based on measurements at the spinel/substrate interface across the plain tube specimen. (For interpretation of the references to colour in this figure legend, the reader is referred to the web version of this article.)

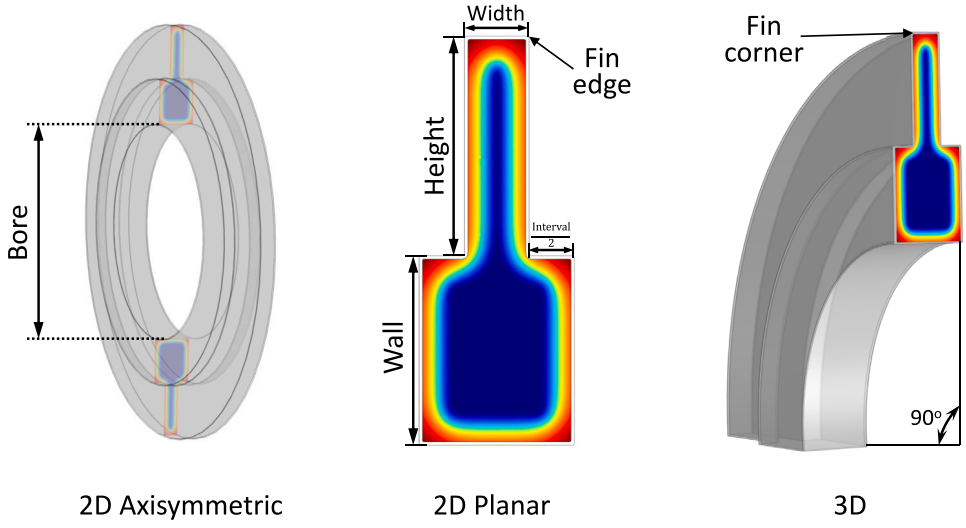


Fig. 12. Geometry of component assumed in the carbon uptake model; oxidation kinetics have been considered for all cases, with the outmost surface (grey) denoting the original gas/substrate interface; the rotational twist representing spiral fins is considered in the 3D case.

here because carbon diffuses through the Cr-depleted matrix of the IOZ rapidly and without reaction; its activity at the IOZ/carburisation zone interface is therefore very little changed from the value at the scale/metal interface. Furthermore, the description of the inward flux of carbon at the spinel/substrate interface (Eq. (2)) is modified by adding an extra 'snow plowing' term which is dependent on the moving velocity of the interface $\boldsymbol{v}^\star$ and the carbon partition coefficient P_C, consistent with:

$$\boldsymbol{J}_C^\star V_m = \alpha_a \{T\} \left(a_C^{eq} - a_C^\star\right) + P_C C_C^\star V_m \boldsymbol{v}^\star \{t\} \tag{6}$$

where $P_C = 0$ means that the spinel retains all the carbon as it grows while $P_C = 1$ means all carbon is piled-up in the substrate ahead of the spinel. Currently, in all assessments, it is assumed that $P_C = 1$, giving rather more aggressive predictions of carbon uptake and thus more conservative lifetime projections. The position of the spinel/substrate interface $z_x^\star$, which gives $\boldsymbol{v}^\star = \mathrm{d}z_x^\star/\mathrm{d}t$, has the following time-dependent analytical form:

$$z_x^\star \{t\} = \beta\sqrt{D_O t + \left(z_x^{\star,\circ}/\beta\right)^2} \tag{7}$$

where $z_x^{\star,\circ}$ is its initial position, D_O is the chemical diffusion coefficient of oxygen in the scale and β is a constant derived from the similarity method. Both $z_x^{\star,\circ}$ and D_O are fitted to measured oxidation rate data (see Section 2.2). Readers are referred to Appendix A Supplementary data for a mathematical derivation of Eq. (7). Such a general treatment of coupling the diffusion of carbon with oxidation kinetics is particularly useful as it allows the simulations to be extended to arbitrary geometries, where the velocity of the moving spinel/substrate interface depends on the local concentration gradient (of 'oxygen') at the interface.

4. Application of models for data analysis

To rationalise the kinetic model for the carbon uptake measurements, a sensitivity analysis has been undertaken to evaluate the assumptions made in determining the carbon diffusion coefficient; the effect of taking into account oxidation kinetics; and the precise geometry of the calculation domain. The fitting (of physical parameters) procedure (to measured carbon profiles) was implemented by using the trust-region nonlinear least square method [41] and the bisquare weights robust least squares method [42].

First, the interface reaction kinetics α_a/V_m is estimated by using the effective carbon diffusion coefficient derived from CalPhaD databases

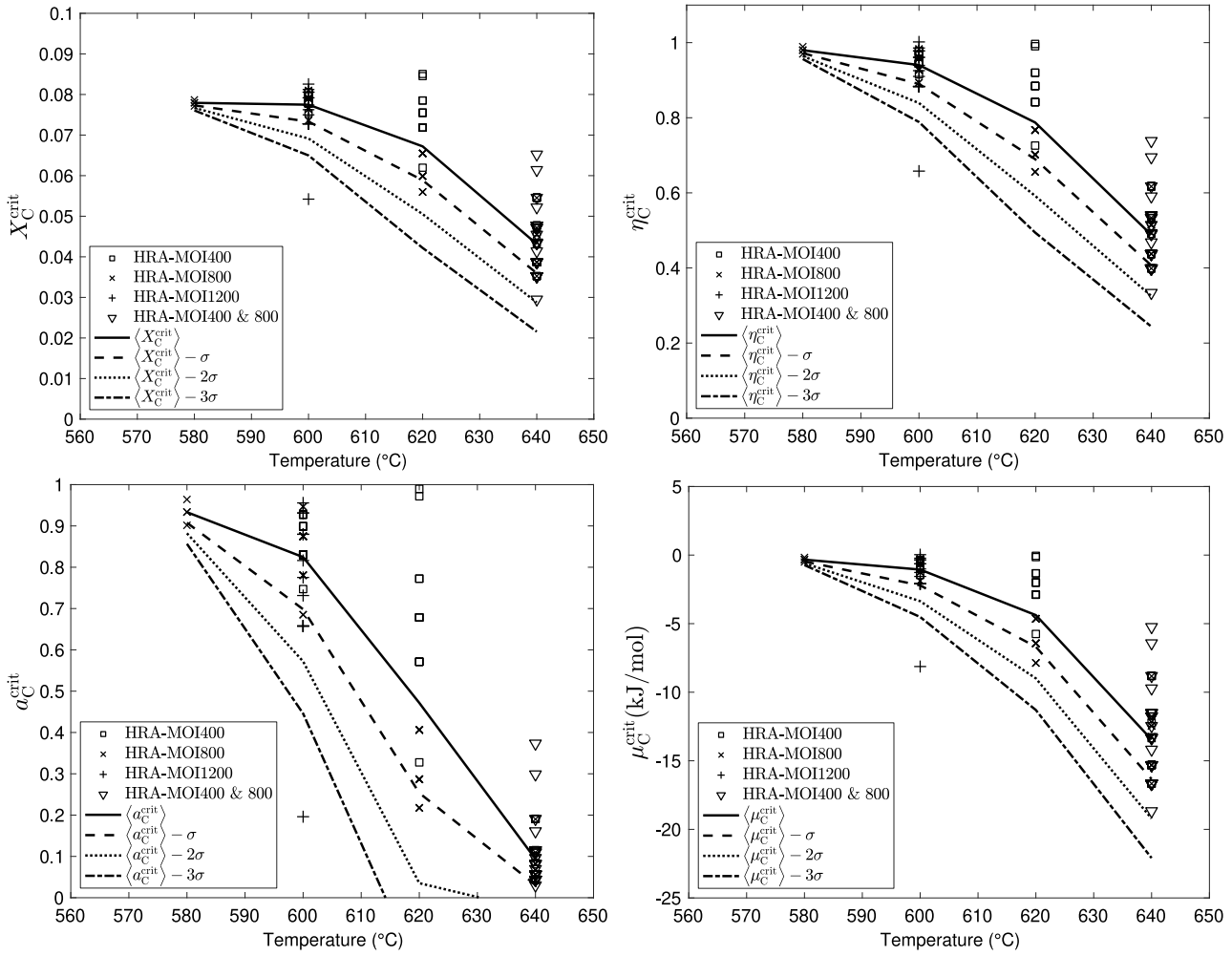


Fig. 13. Calibrated critical X_C, η_C, a_C and μ_C at the spinel/substrate interface; calculations were done taking into account oxidation kinetics.

(following Eq. (4), see values in Fig. 7 for different alloys). An optimum value of α_a/V_m is derived for each measured profile by applying Eqs. (2)–(5). Then, both α_a/V_m and the carbon diffusion coefficient correction factor ζ are adjusted to fit each profile. This gives a better fit to measured profiles at low temperatures where a larger ζ is suggested, see derived values of α_a/V_m and ζ for each sample plotted in Fig. 9. A very good Arrhenius fit of α_a/V_m over the temperature range of 485–640 °C is obtained, as shown in Fig. 9, which is consistent with a thermally-activated Boudouard reaction as proposed theoretically in [30]. Next, the data is fit by assuming ζ to be constant (3, 10 or 50) or to follow the inverse-Arrhenius law represented by the solid line in Fig. 9(b). This allows the influence of chosen value of ζ, which is described empirically in this work, to be analysed. The activation energy Q_α & pre-factor obtained from the Arrhenius fit of Fig. 9(a) for α_a/V_m, and the coefficient of determination values are listed in Table 4 (no oxidation, by fixing the position of scale/alloy interface). One can see that allowing ζ either to be selected at each temperature or to follow the inverse-Arrhenius law gives the better fits. The sequence of calculation has been repeated by also considering the metal loss due to spinel growth. By calibrating Eq. (7) based on the dataset of measured oxide thickness (Fig. 4), the following temperature-dependent expressions for D_O and $z_x^{\star,\circ}$ are derived.

$$D_O\{T\} = 2.65616\times10^{-5}\exp\left\{\frac{-193.3\times10^3[\mathrm{J\,mol^{-1}}]}{RT}\right\}\ \mathrm{m^2\,s^{-1}} \quad (8)$$

$$z_x^{\star,\circ}\{T\} = 9.72946\times10^{-10}\sqrt{\exp\left\{2.32922\times10^{-2}\,T[\mathrm{K}]\right\}}\ \mathrm{m} \quad (9)$$

Table 4
Summary of activation energy [kJ/mol] and pre-factor [mol·m^{-2}·s^{-1}] for derived interface reaction parameter α_a/V_m.

Oxidation	Assumption of ζ	Activation energy	Pre-factor	R^2
Yes	ζ adjusted	221.4	7.87×10^5	0.927
	Inverse Arrhenius law	220.3	6.69×10^5	0.922
	$\zeta = 1$	250.8	3.80×10^7	0.917
	$\zeta = 3$	236.4	6.08×10^6	−0.091
	$\zeta = 10$	232.0	3.62×10^6	−0.083
	$\zeta = 50$	217.3	4.64×10^5	−0.111
No	ζ adjusted	219.6	6.30×10^5	0.929
	Inverse Arrhenius law	218.4	5.23×10^5	0.925
	$\zeta = 1$	240.4	9.63×10^6	−0.077
	$\zeta = 3$	226.0	1.52×10^6	0.937
	$\zeta = 10$	224.2	1.27×10^6	−0.083
	$\zeta = 50$	214.7	3.33×10^5	−0.111

Here no significant effects on the observed oxidation kinetics have been found by changing the gas moisture content; a unified expression describing oxidation is thus used for all exposure gas compositions.

As listed in Table 4 (with oxidation, by allowing the Cr-rich scale to grow inwards), the derived activation energy for the interface reaction Q_α obtained by taking into account oxidation kinetics is approximate 220 kJ mol^{-1}, slightly larger than that without considering oxidation kinetics. Changes in the predicted maximum carbon concentration in the alloy (or degree of carbon uptake, see definition in Eq. (10)) when oxidation kinetics are taken into account are illustrated in Fig. 10;

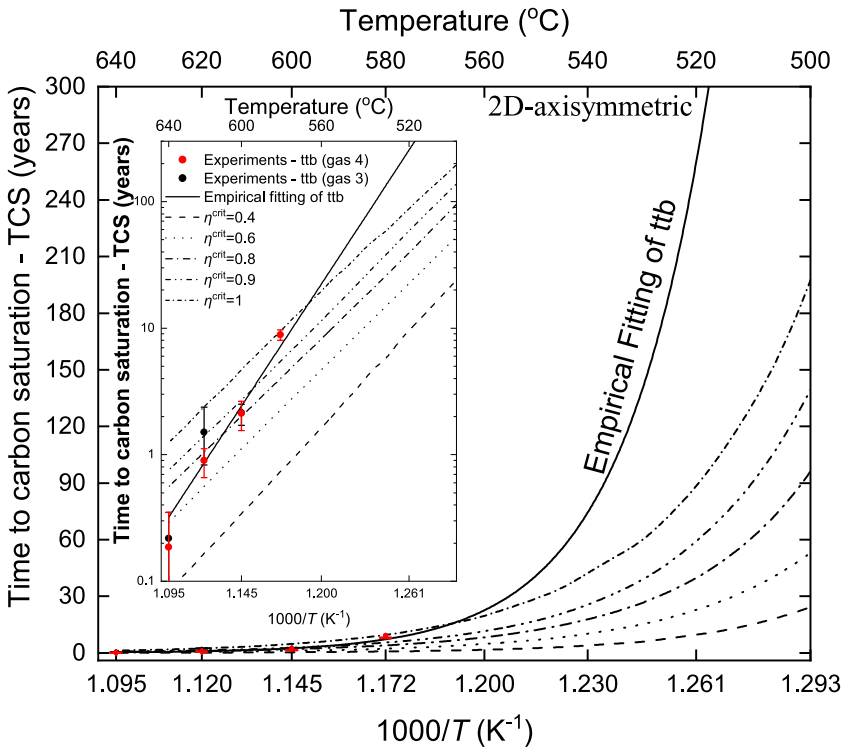


Fig. 14. Predicted time to carbon saturation with different η^{crit} assumed; calculations were done by using the Arrhenius fit of α_a/V_m and inverse-Arrhenius fit of ζ taking into account oxidation kinetics; a 2D axisymmetric geometry is used. Average ttb (taken as half between TTB and TafterB) measured for samples exposed to gas 3 and gas 4 are represented by black and red circles respectively; The error bar indicates the range of measurements between the minimum TTB and the maximum TafterB. (For interpretation of the references to colour in this figure legend, the reader is referred to the web version of this article.)

oxidation is found to accelerate the carburisation kinetics. The calibrated 1D model has been compared with measured carbon content at the spinel/substrate interface (at $t = (1 \pm 0.3)\times 1 \times 10^5$ h) as shown in Fig. 11. Good agreement is found at temperatures of interest to reactor conditions between 480 and 520 °C.

Finally, we consider the effect of geometry. A 1D geometry (for fitting purposes), 2D (planar) and 2D (axisymmetric) geometries are studied, as shown in Fig. 12. Predictions (Fig. 10) suggest more rapid carbon uptake (at the fin edge) in 2D; this is consistent with experimental observations that breakaway initiations generally occur first at fin edges.

5. On the implications for lifetime failure analysis by kinetic modelling

The modelling work reported here has allowed a quantified law for carbon ingress to be proposed on the basis of chemical reaction rate theory backed up by experimental measurements of carbon uptake. The law has been shown to apply across the temperature interval relevant to reactor operation and the higher temperatures used for accelerated corrosion tests on finned samples.

Moreover, it has been demonstrated that some degree of carbon uptake occurs across the full range of temperatures considered. This observation is highly pertinent to modelling the degradation of the Fe9Cr1Mo steel since the carbon concentration field represents a physically-based state variable which can be used to characterise the degree to which the steel has been attacked. When considering the state of degradation of the material, one can argue [8,30] that the degree of carbon uptake by a steel component is critical. It represents progressive loss of the steel's ability to absorb more carbon released by the Boudouard reaction taking place at its surface.

Carbon is produced in reaction (1) at the oxide/metal interface and drained away by diffusion into the steel and carbide precipitation therein. The rates of both carbon generation at the surface (Eq. (2)) and its removal according to Eqs. (3) and (4) slow with time, but according to different rate laws. When diffusion into the partially carburised steel becomes too slow, excess carbon generated by reaction (1) can deposit onto the metal surface, that is to say, within the spinel scale layer. The consequent volume expansion disrupts the scale, destroying its semi-protective character. Because the steel is by then carburised, insufficient chromium remains in the ferrite to heal the scale, and breakaway ensues. This concept is explored using a degree of carbon uptake relative to saturation at the steel/scale interface, η_C, defined as

$$\eta_C = X_C/X_C^{eq} \tag{10}$$

where X_C is the local value for total carbon concentration and X_C^{eq} is the equilibrium carbon mole fraction. Note that η_C has the characteristics of a state variable; one can calculate a critical value η_C^{crit} corresponding to the measured time at which breakaway occurs, at any given temperature.

For each measured ttb and associated exposure conditions at high temperature, $\eta_C^{crit} = X_C^{ttb}/X_C^{eq}$ can be predicted from the kinetic model. Fig. 13 shows calculated values of η_C^{crit} as a function of temperature; related quantities such as the critical carbon activity $a_C^{crit} = a_C^{ttb}/a_C^{eq}$, the critical carbon mole fraction $X_C^{crit} = X_C^{ttb}$ and the critical chemical potential of carbon relative to graphite $\mu_C^{crit} = \mu_C^{ttb} - \mu_C^{eq}$ are also included. The data underlying the calculation is scattered, and lines corresponding to the mean, $-\sigma$, -2σ and -3σ, where σ is the standard deviation, are provided for guidance.

Experimentally measured values of X_C^{crit} are also included in Fig. 13, along with the other critical quantities calculated from them. Scatter in the measured X_C^{crit} values is significant, but almost all measurements fall within one standard deviation of the model predictions. As is seen, the kinetic model also succeeds in describing the temperature dependence of X_C^{crit}. Values of η_C^{crit} are at or close to unity, corresponding to carbon saturation of the steel subsurface region when breakaway occurs at 580 and 600 °C. However, this is not the case at higher temperatures,

where $\eta_C^{crit} < 1$. Nonetheless, breakaway at higher temperatures is accompanied by graphite formation within the spinel layer in contact with the steel surface.

There are two potential explanations for this apparent anomaly. First, the value of a_C outside the steel surface exceeds the boundary value within the steel (Fig. 6, bottom right). In the early stages of the reaction when η_C is small, supersaturation is prevented by carbon dissolution into the metal. Later, as η_C rises, this process is slowed and supersaturation could result in graphite precipitation. Second, and perhaps more importantly, at higher temperatures the rate of steel oxidation also increases. The rapid advance of the scale-alloy interface can engulf Cr-rich carbides into the scale, where they slowly oxidise, releasing carbon [8,43,44]. Both carbide oxidation and carbon precipitation are accompanied by volume expansion, promoting breakaway.

Fig. 14 shows predicted times to reach specified values of carbon uptake at different temperatures, in comparison with measured ttb at high temperatures. As is seen in the inset Arrhenius plot, measured ttb values at high temperatures correspond to low values of η_C^{crit} whereas at 580 °C, carbon saturation ($\eta_C^{crit} = 1$) and breakaway occur together.

An empirical extrapolation of the measured ttb data is shown as a continuous line on Fig. 14 and its inset. Whilst it appears to predict very long steel lifetimes for realistic reactor temperatures, it also corresponds to remarkably high values of η_C^{crit}. Such large degrees of carbon supersaturation are physically unrealistic, given the limited supply of chromium in the steel and low solubility of carbon in ferrite. If instead the criterion of $\eta_C^{crit} = 1$ is adopted for breakaway, more realistic lifetime predictions are arrived at.

It is clear that the predicted times at low temperatures are much shorter than empirical extrapolations made on the basis of an inverse Arrhenius extrapolation of the measured ttb data. This implies a change in mechanistic regime, consistent with the observation [8,43,44] that Cr-rich carbides are incorporated into the oxide scale as a result of its rapid inward growth [45] at high temperatures, whereas at low temperatures, the carbides are oxidised within the steel to produce an IOZ and release carbon back into the ferrite.

The apparent activation energy for breakaway (as estimated from the solid line on the inset of Fig. 13) is higher than that in the carbon ingress model – by about a factor of two. This too reflects the difficulties in predicting the breakaway onset at lower (actual operating) temperatures from high-temperature data. No measured ttb data are available for the low temperatures of interest, but carburisation profiles have been obtained for this regime. As shown here and previously [30], the carbon uptake kinetic model succeeds in predicting carbon profiles over the entire temperature range examined.

It is seen from Fig. 14 that lowering the gas exposure temperature (e.g. from 520 to 500 °C), for the simulations modelled, the predicted effect is to increase the time for carburisation by many decades. For the particular geometry modelled in that figure, reducing the operating temperature doubles the component lifetime. Relatively small temperature changes thus can potentially extend the lifetime of reactor components significantly.

6. Summary and conclusions

The following specific conclusions can be drawn from this work:

- It is shown that breakaway oxidation is associated with extensive precipitation at the metal/scale interface of chromium-rich carbides and an associated carbon activity close to unity — consistent with carbon saturation of the underlying substrate. The associated ferritic matrix is severely depleted with respect to chromium, destroying the semi-protective nature of the scale and leaving it disrupted, unable to heal and thus prone to breakaway oxidation.
- Based on the above, a kinetic model is proposed to describe the carbon uptake in the substrate. The interface at the metal/scale region is treated in a physically realistic way consistent with the Boudouard reaction assuming interface reaction control – the so-called Robin condition – at the moving boundary.
- The interface reaction rate parameter varies by 5 orders of magnitude across the temperature regime considered, consistent with a thermally-activated Boudouard reaction as proposed theoretically in the literature.
- The degree of carbon uptake at breakaway is found to increase towards that needed to support graphitisation at the scale/alloy interface as the temperature is decreased. The apparent activation energy for time-to-breakaway (~400 kJ mol^{-1}) is appreciably greater than that estimated for carbon uptake (~230 kJ mol^{-1}). It is postulated that this may be due to the higher carbon content in the scale caused by the rapid advance of the scale-alloy interface at higher temperatures; volume expansions due to both carbide oxidation and carbon precipitation may be accelerating the kinetics of breakaway.
- Although the breakaway effect has never been observed at temperatures associated with nuclear reactor conditions, carbon uptake is observed across the entire temperature regime of interest. On this basis it is concluded that the degree of carbon uptake is a reasonable physical measure of damage. The models presented here allow this to be determined, and their application may be suitable for remnant lifetime analysis to support nuclear plant lifetime extension strategies.

CRediT authorship contribution statement

Yilun Gong: Conceptualization, Methodology, Software, Formal analysis, Investigation, Writing – original draft, Writing – review & editing. **Simon P.A. Gill:** Software, Validation, Investigation. **Sabrina Yan:** Investigation. **Rebecca Higginson:** Investigation. **Joy Sumner:** Investigation. **Nigel J. Simms:** Investigation. **Henrik Larsson:** Software, Validation, Investigation. **Aya Shin:** Resources, Investigation, Project administration, Funding acquisition. **Jonathan M. Pearson:** Resources, Investigation, Project administration, Funding acquisition. **David J. Young:** Investigation, Writing – review & editing. **Colin Atkinson:** Formal analysis, Writing – review & editing, Supervision. **Alan C.F. Cocks:** Conceptualization, Investigation, Validation, Writing – original draft, Writing – review & editing, Supervision. **Roger C. Reed:** Conceptualization, Investigation, Funding acquisition, Writing – original draft, Writing – review & editing, Supervision.

Declaration of competing interest

The authors declare that they have no known competing financial interests or personal relationships that could have appeared to influence the work reported in this paper.

Data availability

The data that supports the findings of this study are available on request from the corresponding author. Part of the background information is not available due to confidentiality.

Acknowledgements

The authors kindly thank EDF Energy Nuclear Generation Limited, UK for the provision of funding, TGA data and experimental specimens, and Jacobs for the experimental support.

Appendix A. Supplementary data

Supplementary material related to this article can be found online at https://doi.org/10.1016/j.corsci.2023.111385.

References

[1] D.J. Young, High Temperature Oxidation and Corrosion of Metals, second ed., Elsevier, 2016, http://dx.doi.org/10.1016/C2014-0-00259-6.

[2] R. Allam, S. Martin, B. Forrest, J. Fetvedt, X. Lu, D. Freed, G.W. Brown Jr., T. Sasaki, M. Itoh, J. Manning, Demonstration of the Allam cycle: An update on the development status of a high efficiency supercritical carbon dioxide power process employing full carbon capture, Energy Procedia 114 (2017) 5948–5966, http://dx.doi.org/10.1016/j.egypro.2017.03.1731.

[3] R. Chacartegui, J.M. De Escalona, D. Sánchez, B. Monje, T. Sánchez, Alternative cycles based on carbon dioxide for central receiver solar power plants, Appl. Therm. Eng. 31 (2011) 872–879, http://dx.doi.org/10.1016/j.applthermaleng.2010.11.008.

[4] R.G. Brese, J.R. Keiser, B.A. Pint, Effect of thermal cycling on compatibility in CO2 for concentrated solar power applications, Oxid. Met. 87 (2017) 631–642, http://dx.doi.org/10.1007/s11085-017-9762-0.

[5] Y. Cai, T.D. Nguyen, J. Zhang, B. Gleeson, D.J. Young, Corrosion behaviour of Fe-based austenitic and Ni-based alloys in wet CO2 gas with and without chloride deposits at 650 °C, Corros. Sci. 210 (2023) 110822, http://dx.doi.org/10.1016/j.corsci.2022.110822.

[6] V. Dostal, P. Hejzlar, M.J. Driscoll, High-performance supercritical carbon dioxide cycle for next-generation nuclear reactors, Nucl. Technol. 154 (2006) 265–282, http://dx.doi.org/10.13182/NT154-265.

[7] World Nuclear News, UK nuclear plant gets ten-year extension, 2015, http://www.world-nuclear-news.org/C-UK-nuclear-plant-gets-ten-year-extension-2001157.html. (Accessed 28 September 2016).

[8] Y. Gong, D.J. Young, P. Kontis, Y.L. Chiu, H. Larsson, A. Shin, J.M. Pearson, M.P. Moody, R.C. Reed, On the breakaway oxidation of Fe9Cr1Mo steel in high pressure CO_2, Acta Mater. 130 (2017) 361–374, http://dx.doi.org/10.1016/j.actamat.2017.02.034.

[9] World Nuclear News, EDF to extend Heysham 1 and Hartlepool for two extra years, 2023, https://www.world-nuclear-news.org/Articles/EDF-to-extend-Heysham-1-and-Hartlepool-for-two-ext. (Accessed 10 March 2023).

[10] E. Musk, Making humans a multi-planetary species, New Space 5 (2017) 46–61, http://dx.doi.org/10.1089/space.2017.29009.emu.

[11] E. Musk, Making life multi-planetary, New Space 6 (2018) 2–11, http://dx.doi.org/10.1089/space.2018.29013.emu.

[12] G.C.C. Costa, N.S. Jacobson, D. Lukco, G.W. Hunter, L. Nakley, B.G. Radoman-Shaw, R.P. Harvey, Oxidation behavior of stainless steels 304 and 316 under the Venus atmospheric surface conditions, Corros. Sci. 132 (2018) 260–271, http://dx.doi.org/10.1016/j.corsci.2018.01.002.

[13] Z. Shen, D. Tweddle, H. Yu, G. He, A. Varambhia, P. Karamched, F. Hofmann, A.J. Wilkinson, M.P. Moody, L. Zhang, S. Lozano-Perez, Microstructural understanding of the oxidation of an austenitic stainless steel in high-temperature steam through advanced characterization, Acta Mater. 194 (2020) 321–336, http://dx.doi.org/10.1016/j.actamat.2020.05.010.

[14] Z. Shen, K. Chen, H. Yu, B. Jenkins, Y. Ren, N. Saravanan, G. He, X. Luo, P.A.J. Bagot, M.P. Moody, L. Zhang, S. Lozano-Perez, New insights into the oxidation mechanisms of a Ferritic-Martensitic steel in high-temperature steam, Acta Mater. 194 (2020) 522–539, http://dx.doi.org/10.1016/j.actamat.2020.05.052.

[15] Z. Shen, J. Zhang, S. Wu, X. Luo, B.M. Jenkins, M.P. Moody, S. Lozano-Perez, X. Zeng, Microstructure understanding of high Cr-Ni austenitic steel corrosion in high-temperature steam, Acta Mater. 226 (2022) 117634, http://dx.doi.org/10.1016/j.actamat.2022.117634.

[16] F. Rouillard, G. Moine, L. Martinelli, J.C. Ruiz, Corrosion of 9Cr steel in CO_2 at intermediate temperature I: Mechanism of void-induced duplex oxide formation, Oxid. Met. 77 (2012) 27–55, http://dx.doi.org/10.1007/s11085-011-9271-5.

[17] F. Rouillard, G. Moine, M. Tabarant, J.C. Ruiz, Corrosion of 9Cr steel in CO_2 at intermediate temperature II: Mechanism of carburization, Oxid. Met. 77 (2012) 57–70, http://dx.doi.org/10.1007/s11085-011-9272-4.

[18] D.J. Young, T.D. Nguyen, P. Felfer, J. Zhang, J.M. Cairney, Penetration of protective chromia scales by carbon, Scr. Mater. 77 (2014) 29–32, http://dx.doi.org/10.1016/j.scriptamat.2014.01.009.

[19] D.J. Young, P. Huczkowski, T. Olszewski, T. Hüttel, L. Singheiser, W.J. Quadakkers, Non-steady state carburisation of martensitic 9-12%Cr steels in CO_2 rich gases at 550 °C, Corros. Sci. 88 (2014) 161–169, http://dx.doi.org/10.1016/j.corsci.2014.07.024.

[20] K.E. Nygren, Z. Yu, F. Rouillard, A. Couet, Effect of sample thickness on the oxidation and carburization kinetics of 9Cr-1Mo steel in high and atmospheric pressure CO2 at 550 °C, Corros. Sci. 163 (2020) 108292, http://dx.doi.org/10.1016/j.corsci.2019.108292.

[21] A. Shin, M. Chevalier, E. Laney, J. Pearson, Oxidation behaviour of steels in advanced gas cooled reactors, Mater. High Temp. 35 (2018) 1–9, http://dx.doi.org/10.1080/09603409.2017.1389114.

[22] F. Jones, J. Rosser, Review of 9Cr Oxidation Data: Protective and Weight Gain at Breakaway, Technical Report E/REP/BPKB/0191/AGR/16, Revision 001, Frazer-Nash Consultancy on behalf of EDF Energy, 2018.

[23] R.A. Brierley, D.A. Cox, First Progress Report on the Oxidation Testing of Hartlepool - Heysham Production 9Cr-1Mo Finned Boiler Tube Materials, Tech. Rep., British Nuclear Design & Construction Limited, 1974.

[24] G.L.R. Durber, R.A. Brierley, The Oxidation of Heysham Production 9Cr-1Mo Plain Boiler Tubing in Simulated C.A.G.R. Environments, Tech. Rep., Nuclear Power Company (Whetstone) Limited, 1976, NPC(W)/R.89.

[25] J. Sumner, N. Simms, A. Shin, J. Pearson, Kinetics of duplex oxide growth on 9Cr steels exposed in CO_2: Application of dimensional metrology, Oxid. Met. 87 (2017) 617–629, http://dx.doi.org/10.1007/s11085-017-9766-9.

[26] R.A. Brierley, Oxidation Testing of Hartlepool/Heysham1 9Cr Boiler Tube Materials in CAGR Environments At the then NNC - Summary Report to End of Tests, Tech. Rep., Wood, 2019.

[27] L. Coghlan, S. Yan, A. Shin, J. Pearson, M.A.E. Jepson, R.L. Higginson, Dispersion of complex carbides at the oxidation front during the oxidation of 9Cr-1Mo steel, Corros. Sci. 165 (2020) 108389, http://dx.doi.org/10.1016/j.corsci.2019.108389.

[28] L. Coghlan, S. Yan, A. Shin, J. Pearson, M.A.E. Jepson, R.L. Higginson, The effect of microstructure on the oxidation and carburisation of 9Cr-1Mo steel exposed to CO2, Corros. Sci. 191 (2021) 109720, http://dx.doi.org/10.1016/j.corsci.2021.109720.

[29] S. Yan, S. Doak, R. Thomson, R. Higginson, An investigation on oxidation/carburisation of 9Cr-1Mo steel heat exchanger tube in an AGR environment, Mater. High Temp. 35 (2018) 56–65, http://dx.doi.org/10.1080/09603409.2017.1392411.

[30] Y. Gong, D.J. Young, C. Atkinson, T. Olszewski, W.J. Quadakkers, R.C. Reed, Modelling of the degradation of martensitic stainless steels by the boudouard reaction, Corros. Sci. 173 (2020) 108699, http://dx.doi.org/10.1016/j.corsci.2020.108699.

[31] D.J. Young, J. Zhang, Corrosion by hot CO_2 gases, Electrochem. Soc. Interface 30 (2021) 73–77, http://dx.doi.org/10.1149/2.f08212if.

[32] H. Larsson, A. Engström, A homogenization approach to diffusion simulations applied to $\alpha+\gamma$ Fe-Cr-Ni diffusion couples, Acta Mater. 54 (2006) 2431–2439, http://dx.doi.org/10.1016/j.actamat.2006.01.020.

[33] H. Larsson, H. Strandlund, M. Hillert, Unified treatment of Kirkendall shift and migration of phase interfaces, Acta Mater. 54 (2006) 945–951, http://dx.doi.org/10.1016/j.actamat.2005.10.022.

[34] H. Larsson, L. Höglund, Multiphase diffusion simulations in 1D using the DICTRA homogenization model, CALPHAD 33 (2009) 495–501, http://dx.doi.org/10.1016/j.calphad.2009.06.004.

[35] Y. Gong, Modelling of Diffusional Phenomena in Structural Alloys for High Temperature Applications (Ph.D. thesis), University of Oxford, 2017.

[36] H.E. McCOY, Type 304 stainless steel vs flowing CO2 at atmospheric pressure and 1100-1800f, Corrosion 21 (1965) 84–94, http://dx.doi.org/10.5006/0010-9312-21.3.84.

[37] C.T. Fujii, R.A. Meussner, Carburization of Fe-Cr alloys during oxidation in dry carbon dioxide, J. Electrochem. Soc. 114 (1967) 435, http://dx.doi.org/10.1149/1.2426622.

[38] D.R. Holmes, R. Hill, L.M. Wyatt (Eds.), British nuclear energy society (BNES) international conference on corrosion of steels in CO_2, in: British Nuclear Energy Society, BNES International Conference on Corrosion of Steels in CO_2, 1974.

[39] C. Wagner, Theoretical analysis of the diffusion processes determining the oxidation rate of alloys, J. Electrochem. Soc. 99 (1952) 369–380, http://dx.doi.org/10.1149/1.2779605.

[40] H. Larsson, T. Jonsson, R. Naraghi, Y. Gong, R.C. Reed, J. Ågren, Oxidation of iron at 600 °C– Experiments and simulations, Mater. Corros. 68 (2017) 133–142, http://dx.doi.org/10.1002/maco.201508781.

[41] J.J. Moré, D.C. Sorensen, Computing a trust region step, SIAM J. Sci. Stat. Comput. 4 (1983) 553–572, http://dx.doi.org/10.1137/0904038.

[42] W. Dumouchel, F. O'Brien, Integrating a robust option into a multiple regression computing environment, in: Computing and Graphics in Statistics, Springer-Verlag New York, Inc., 1992, pp. 41–48.

[43] J.P. Abellán, T. Olszewski, G.H. Meier, L. Singheiser, W.J. Quadakkers, The oxidation behaviour of the 9%Cr steel P92 in CO_2- and H_2O-rich gases relevant to oxyfuel environments, Int. J. Mater. Res. 101 (2010) 287–299, http://dx.doi.org/10.3139/146.110271.

[44] T.D. Nguyen, J. Zhang, D.J. Young, Effects of cerium and manganese on corrosion of Fe-Cr and Fe–Cr–Ni alloys in Ar–20CO_2 and Ar–20CO_2–20H_2O gases at 650 °C, Corros. Sci. 100 (2015) 448–465, http://dx.doi.org/10.1016/j.corsci.2015.08.012.

[45] M.R. Taylor, J.M. Calvert, D.G. Lees, D.B. Meadowcroft, The mechanism of corrosion of Fe-9%Cr alloys in carbon dioxide, Oxid. Met. 14 (1980) 499, http://dx.doi.org/10.1007/BF00603476.



https://dspace.org/

Assessment of corrosive attack of Fe9Cr1Mo alloys in pressurised CO2 for prediction of breakaway oxidation

Gong, Yilun; Gill, Simon P. A.; Yan, Sabrina; Higginson, Rebecca; Sumner, Joy ...

2023-09-01
Elsevier
https://doi.org/10.1016/j.corsci.2023.111385
Gong Y, Gill SPA, Yan S, et al., (2023) Assessment of corrosive attack of Fe9Cr1Mo alloys in pressurised CO2 for prediction of breakaway oxidation. Corrosion Science, Volume 222, September 2023, Article number 111385

Downloaded from a DSpace repository. https://dspace.org/